



# High water solubility of ringwoodite at mantle transition zone temperature

HPSTAR  
906-2020

Hongzhan Fei<sup>a,\*</sup>, Tomoo Katsura<sup>a,b</sup>

<sup>a</sup> Bayerisches Geoinstitut, University of Bayreuth, Bayreuth D95440, Germany

<sup>b</sup> Center for High Pressure Science and Technology Advanced Research, Beijing 100094, China

## ARTICLE INFO

### Article history:

Received 18 September 2019

Received in revised form 16 November 2019

Accepted 26 November 2019

Available online xxxx

Editor: J. Brodholt

### Keywords:

H<sub>2</sub>O solubility

ringwoodite

mantle transition zone

## ABSTRACT

The mantle transition zone, a potential water reservoir in the Earth's interior, is suggested to contain more than 1 wt.% of H<sub>2</sub>O, at least locally, by the natural water-rich ringwoodite inclusion (Pearson et al., 2014) and the mineral viscosity (Fei et al., 2017). It is against the low H<sub>2</sub>O solubility of ringwoodite (< 0.3 wt.%) at mantle transition zone temperature based on laboratory experiments (Ohtani et al., 2000). We revisited the H<sub>2</sub>O solubility in ringwoodite at 1600–2000 K, showing that both iron-free and iron-bearing ringwoodite can store about 0.8–1.2 wt.% of H<sub>2</sub>O under mantle transition zone conditions. Temperature has a relatively small effect on the H<sub>2</sub>O solubility in iron-bearing system, but much larger in iron-free one. The high H<sub>2</sub>O solubility of ringwoodite is compatible with the water-rich mantle transition zone. The relatively low values reported previously is probably due to insufficient H<sub>2</sub>O source or unbuffered by SiO<sub>2</sub>.

© 2019 Elsevier B.V. All rights reserved.

## 1. Introduction

The mantle transition zone at 410–660 km depths is widely accepted as a potential water reservoir in the Earth's interior (e.g., Bercovici and Karato, 2003; Hirschmann, 2006; Tschauner et al., 2018) because its dominant minerals, wadsleyite and ringwoodite, can store up to 2.7 wt.% of H<sub>2</sub>O in their crystal structures as hydroxyl (Kohlstedt et al., 1996). Although various estimations of H<sub>2</sub>O contents (e.g., electrical conductivity; mineral viscosity; and seismic velocity) in the mantle transition zone range from less than 0.1 to 2 wt.% (e.g., Fei et al., 2017; Houser, 2016; Kelbert et al., 2009; Thio et al., 2016; Yoshino et al., 2008), comparisons of mineral viscosity data with geophysical observations (e.g., Fei et al., 2017) and the recently discovered ringwoodite inclusion with ~1.4 wt.% H<sub>2</sub>O in a diamond (Pearson et al., 2014) clearly demonstrated a water-rich mantle transition zone, at least locally.

On the other hand, laboratory experiments suggested that, the H<sub>2</sub>O solubility, which is defined as the maximum amount of H<sub>2</sub>O that can be stored within a crystal that coexisted with hydrous melt, of wadsleyite and ringwoodite significantly decreases with increasing temperature (Demouchy et al., 2005; Litasov et al., 2011; Ohtani et al., 2000). By applying the typical geotherm, which is 1950 ~ 2000 K in the lower part of mantle transition zone from

520 to 660 km depth (Katsura et al., 2010), the solubility of H<sub>2</sub>O in ringwoodite is only 0.3 wt.% (Ohtani et al., 2000). It would rule out the possibility of  $\geq 1$  wt.% H<sub>2</sub>O in the mantle transition zone.

The above arguments imply that the H<sub>2</sub>O solubility in ringwoodite at transition zone temperature might have been underestimated. We note that the experimental studies reporting low H<sub>2</sub>O solubility used Fe-free Mg<sub>2</sub>SiO<sub>4</sub> starting materials with 5 wt.% initial bulk H<sub>2</sub>O content (hereafter initial H<sub>2</sub>O) and without an SiO<sub>2</sub> buffer (Ohtani et al., 2000). There are two possibilities causing the underestimation: 1) Fe-bearing ringwoodite may have significantly higher H<sub>2</sub>O solubility than Fe-free one, as the Fe effect on the H<sub>2</sub>O solubility is currently unknown. 2) The 5 wt.% initial H<sub>2</sub>O might be insufficient to saturate ringwoodite, as when ringwoodite coexisted only with hydrous melt and no other solid phases, there is a potential H<sub>2</sub>O content variation in ringwoodite and melt based on the phase rule. Essentially, Fe-free ringwoodite with 2.2 and 0.8 wt.% H<sub>2</sub>O, respectively, were synthesized at 1570 K from starting materials with 11.2 and 5 wt.% initial H<sub>2</sub>O (Bolfan-Casanova et al., 2000; Inoue et al., 1998).

To clarify the H<sub>2</sub>O solubility of ringwoodite under mantle transition zone conditions, we measured the H<sub>2</sub>O contents in both Fe-free and Fe-bearing ringwoodite synthesized at 1600–2000 K with 1.5–22 wt.% initial H<sub>2</sub>O and coexisted with akimotoite + hydrous melt. Our results show that ringwoodite can store ~0.8–1.2 wt.% H<sub>2</sub>O at transition zone temperature, which agrees to the water-rich mantle transition zone inferred from mineral viscosity (Fei et al., 2017) and the natural inclusion (Pearson et al., 2014).

\* Corresponding author.

E-mail address: [hongzhan.fe@uni-bayreuth.de](mailto:hongzhan.fe@uni-bayreuth.de) (H. Fei).

**Table 1**

A list of run conditions, coexisted phases, sample thickness for FTIR, and  $C_{H_2O}^{FW}$  in ringwoodite. All experiments were conducted at 23 GPa. The  $C_{H_2O}^{FW}$  for each run is the average from 6–8 FTIR spectra with one standard deviation.  $T$ : temperature.  $t$ : annealing duration. Rw: ringwoodite. Aki: akimotoite. Melt: quenched crystallized melt. St: stishovite.

	Starting composition <sup>*1</sup>	Run. No.	$T$ (K)	$t$ (min)	Presented phases	Thickness for FTIR ( $\mu\text{m}$ )	$C_{H_2O}^{FW}$ (wt.%) <sup>*4</sup>	$C_{H_2O}^{RW}$ (wt.%) <sup>*5</sup>
Fo100	Mg <sub>2</sub> SiO <sub>4</sub> +5%H <sub>2</sub> O (a)	H4775	2000	300	Rw+melt	49	0.58 (3)	0.49 (2)
		H4784L <sup>*2</sup>	1800	300	Rw+melt	49	1.33(5)	1.12 (4)
	Mg <sub>2</sub> SiO <sub>4</sub> +15%H <sub>2</sub> O (b)	H4805	2000	300	Rw+melt	53	1.03 (4)	0.87 (4)
		H4784H <sup>*2</sup>	1800	300	Rw+Aki+melt	40	2.06 (3)	1.74 (3)
	Mg <sub>2</sub> Si <sub>1.1</sub> O <sub>4.2</sub> +5%H <sub>2</sub> O (c)	H4793	2000	300	Rw+Aki+melt	60	1.06 (6)	0.89 (5)
		H4800	1800	300	Rw+Aki+melt	54	2.03 (13)	1.71 (11)
Fo90	Mg <sub>1.8</sub> Fe <sub>0.2</sub> SiO <sub>4</sub> +1.5%H <sub>2</sub> O	H4754	2000	300	Rw+Aki+melt	72	0.25 (2)	0.18 (1)
		H4711	2000	240	Rw+Aki+melt	43	0.38 (1)	0.28 (1)
	Mg <sub>1.8</sub> Fe <sub>0.2</sub> SiO <sub>4</sub> +5%H <sub>2</sub> O	S6985	1800	40	Rw+Aki+melt	43	0.43 (2)	0.31 (2)
		H4698	2000	120	Rw+Aki+melt	47	1.19 (3)	0.87 (2)
		S7011	2000	180	Rw+Aki+melt	46	1.15 (11)	0.84 (8)
	Mg <sub>1.8</sub> Fe <sub>0.2</sub> SiO <sub>4</sub> +15%H <sub>2</sub> O	H4723	1800	180	Rw+Aki+melt	40	1.31 (8)	0.96 (6)
		H4720	1600	300	Rw+Aki+melt+st	37	1.50 (6)	1.09 (4)
		S7051	2000	240	Rw+Aki?+melt <sup>*3</sup>	43	1.11 (4)	0.81 (3)
	Fo75	Mg <sub>1.5</sub> Fe <sub>0.5</sub> SiO <sub>4</sub> +15%H <sub>2</sub> O	H4762	2000	300	Rw+melt+st	42	1.15 (7)

<sup>\*1</sup>: The starting composition is 100 wt.% silicate plus 1.5, 5, 15, and 22 wt.% H<sub>2</sub>O, namely, the bulk H<sub>2</sub>O content is 1.47 – 18.07 wt.%.

<sup>\*2</sup>: Two capsules with different starting materials were placed within the same assembly in this run.

<sup>\*3</sup>: The akimotoite in S7051 was not observed directly, nevertheless, some part of the sample in the capsule was lost during cross section preparation.

<sup>\*4</sup>: The  $C_{H_2O}^{FW}$  is calculated with Koch-Müller and Rhede (2010) calibration, i.e.,  $\epsilon = 100,000 \text{ L}\cdot\text{mol}^{-1}\cdot\text{cm}^{-2}$  in Eq. (1) for Fo100 samples and  $98,600 \text{ L}\cdot\text{mol}^{-1}\cdot\text{cm}^{-2}$  for Fo90 samples.

<sup>\*5</sup>: The  $C_{H_2O}^{RW}$  is calculated with Bolfan-Casanova et al. (2018) calibration, i.e.,  $\epsilon = 118,500$  and  $135,000 \text{ L}\cdot\text{mol}^{-1}\cdot\text{cm}^{-2}$  for Fe-free and Fe-bearing ringwoodite, respectively, and insensitive to iron content in Fe-bearing system.

## 2. Experimental and analytical methods

### 2.1. 2.1 Starting material and capsulation

MgO, SiO<sub>2</sub>, FeO, and Mg(OH)<sub>2</sub> powders (> 99.9% purity), which were dried at 1370 K (MgO and SiO<sub>2</sub>) or 400 K [FeO and Mg(OH)<sub>2</sub>] prior to weighting, were used as starting materials. By grinding in ethanol, mixtures with bulk compositions of Mg<sub>1.8</sub>Fe<sub>0.2</sub>SiO<sub>4</sub> (Fo90), Mg<sub>1.5</sub>Fe<sub>0.5</sub>SiO<sub>4</sub> (Fo75), Mg<sub>2</sub>SiO<sub>4</sub> (Fo100), and Mg<sub>2</sub>Si<sub>1.1</sub>O<sub>4.2</sub> (to ensure the SiO<sub>2</sub> rich condition) plus 1.5 – 22 wt.% H<sub>2</sub>O were obtained (100 wt.% silicate plus 1.5 to 22 wt.% H<sub>2</sub>O, so the bulk H<sub>2</sub>O contents were 1.47 – 18.1 wt.%) (Table 1). After drying in a vacuum furnace at 400 K to remove ethanol and moisture, the mixtures were sealed in Pt-Rh (5 wt.% Rh) capsules with inner diameter of 1.0 mm and outer diameter of 1.2 mm by arc welding. All the capsule lengths were carefully controlled at 1.2–1.3 mm after welding to reduce the temperature inhomogeneity and uncertainty in high-pressure experiments.

### 2.2. High pressure experiments

Each capsule was loaded into an MgO sleeve and placed in a LaCrO<sub>3</sub> furnace within a ZrO<sub>2</sub> thermal insulator. A Cr<sub>2</sub>O<sub>3</sub>-doped MgO octahedron with edge length of 10 mm was used as pressure medium (standard 10/4 cell assembly at the Bayerisches Geoinstitut). A D-type thermocouple (W<sub>97</sub>Re<sub>3</sub>-W<sub>75</sub>Re<sub>25</sub>) was used to measure the temperature of the capsule. The cell assembly was compressed to 23 GPa at ambient temperature using Kawai-type multi anvil apparatus and heated up to the target temperature (1600 – 2000 K) at a rate of  $\sim 100 \text{ K}/\text{min}$ . After annealing at the target temperature for 40–300 min, which is sufficiently long for the hydrogen equilibrium in ringwoodite (Sun et al., 2015), the assembly was quenched to room temperature by cutting off the heating power, and decompressed to ambient pressure over 15 h. A list of run conditions is given in Table 1.

### 2.3. Sample analyses

#### 2.3.1. Scanning electron microscopy (SEM)

SEM analyses were performed on the cross sections of the recovered samples using the backscattering detector (BSE) with an acceleration voltage of 20 kV and the Energy-dispersive detector (EDS) accelerated with 15 kV voltage. The run products in the capsules appeared as coexisting of 100–500  $\mu\text{m}$  crystals and quenched crystallized melts (Fig. 1a). SEM-EDS analyses showed the chemical compositions of the solid parts as (Mg,Fe)<sub>2</sub>SiO<sub>4</sub> and (Mg,Fe)SiO<sub>3</sub> crystals (and SiO<sub>2</sub> in Run H4720).

#### 2.3.2. Micro focus X-ray diffraction (XRD)

X-ray diffraction patterns were taken on the recovered samples using a micro focused X-ray diffractometer (Bruker AXS D8 Discover) equipped with a two dimensional solid state detector and a micro focus source of Co-K $\alpha$  radiation operated at 40 kV and 500  $\mu\text{A}$ . Ringwoodite can be clearly identified in the solid part as the major phase and akimotoite as the secondary phase. The melt was identified as ringwoodite and phase E, both of which were probably formed by crystallization during quenching, in addition to Pt from the capsule due to the limited space resolution of the diffractometer (Fig. 1b).

#### 2.3.3. Infrared analysis

The recovered capsules were double-side polished to a thickness of 37–72  $\mu\text{m}$  (until no noisy infrared peaks at  $\sim 3120 \text{ cm}^{-1}$ ). Fourier transformation infrared spectroscopy (FTIR) spectra were taken on the ringwoodite grains by a Bruker IFS 120 high-resolution spectrometer coupled with a Bruker IR microscope. One or two hundred scans were accumulated for each spectrum at a resolution of  $2 \text{ cm}^{-1}$ . Six to eight spectra for each sample were obtained on different regions within the same grain and different grains within the same capsule. By adjusting the aperture size (45 to 150  $\mu\text{m}$ ), grain boundaries, cracks, or optically visible inclusions were avoided in each analysis. Examples of the FTIR spectra were shown in Fig. 2.

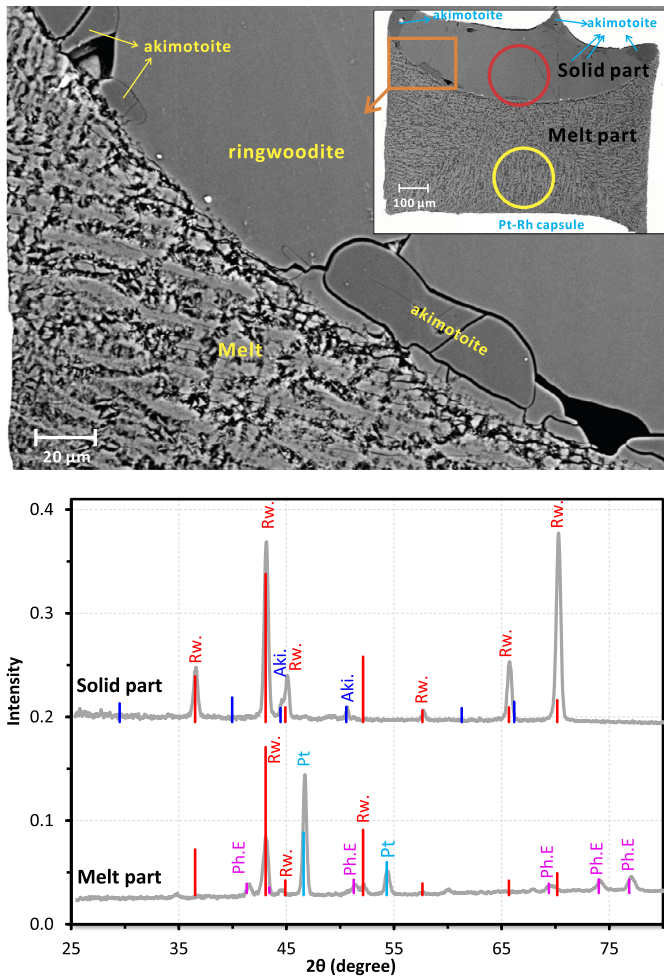


**Fig. 1.** Run product characterization by scanning electron microscope (SEM) and X-ray diffraction (run S7011). (a) Backscattered scanning electron microscope image. (b) X-ray diffraction patterns by micro focused diffractometer on the red (solid part) and yellow (melt part) regions in (a). Rw.: ringwoodite. Aki.: akimotoite. Ph.E: phase E, formed probably during quenching. Pt: from the capsule due to the limited space resolution of the X-ray diffractometer. (For interpretation of the colors in the figure(s), the reader is referred to the web version of this article.)

After baseline subtraction (example of baseline correction is given in Fig. 3 for various H<sub>2</sub>O content samples), the H<sub>2</sub>O contents in ringwoodite (C<sub>H<sub>2</sub>O</sub><sup>rw</sup>) were calculated using the Beer-Lambert law in the form,

$$C_{\text{H}_2\text{O}}^{\text{rw}} = 10^6 \times \int \frac{3A(\nu)M_{\text{H}_2\text{O}}}{\varepsilon\tau\rho} d\nu \quad (1)$$

where C<sub>H<sub>2</sub>O</sub><sup>rw</sup> is the H<sub>2</sub>O content in wt. ppm, A(ν) is the infrared absorption at wavenumber ν, M<sub>H<sub>2</sub>O</sub> is the molar weight of H<sub>2</sub>O (18.02 g/mol), ε is the infrared absorption coefficient [ε = 100,000 and 98,600 L·mol<sup>-1</sup>·cm<sup>-2</sup> for Fe-free and Fe-bearing samples, respectively (Koch-Müller and Rhede, 2010)], τ is sample thickness (normalized to 1 cm in Fig. 2), and ρ is the density [3650 g·L<sup>-1</sup> (Jacobsen et al., 2004)]. The integration was performed for the wavenumber range of 2400 to 4000 cm<sup>-1</sup>.

Note that Koch-Müller and Rhede (2010)'s FTIR calibration is based on secondary ion mass spectrometry (SIMS) data. Recently, Bolfan-Casanova et al. (2018) reported ε = 118,500 L·mol<sup>-1</sup>·cm<sup>-2</sup> for Fe-free ringwoodite and 135,000 L·mol<sup>-1</sup>·cm<sup>-2</sup> for Fe-bearing ringwoodite based on elastic recoil detection analysis (ERDA). By using Bolfan-Casanova et al. (2018)'s calibration, the C<sub>H<sub>2</sub>O</sub><sup>rw</sup> values will be lower by 16% (Fe-free) or 27% (Fe-bearing) as listed in Table 1 for comparison.

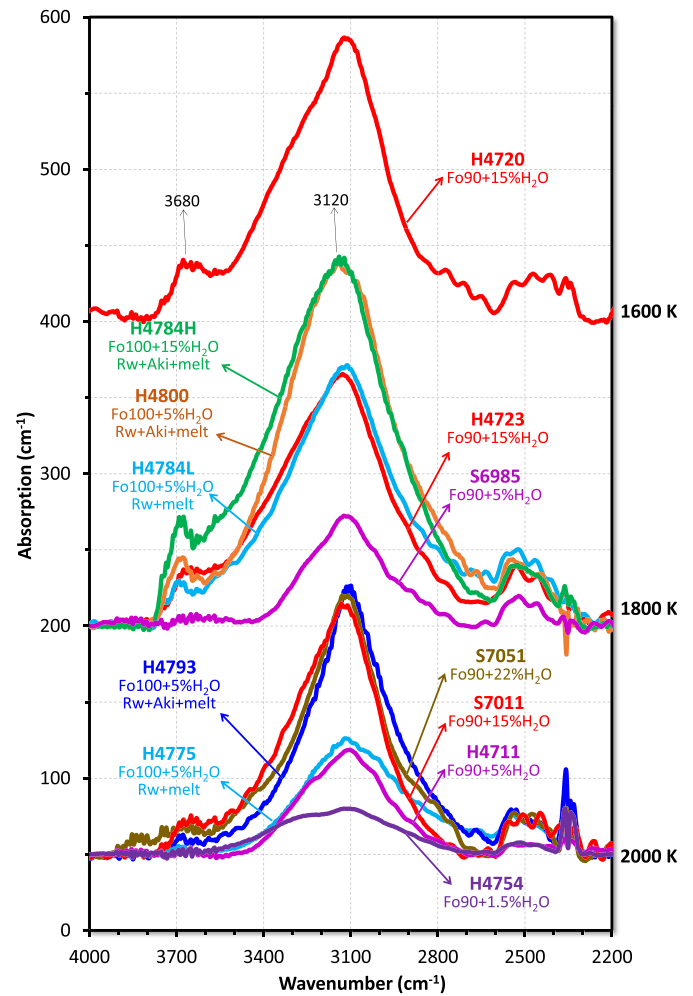


**Fig. 2.** Examples of FTIR spectra after baseline subtraction and thickness normalization to 1 cm. The absorption at ~2340 cm<sup>-1</sup> is caused by CO<sub>2</sub> in the atmosphere. All the spectra were vertically shifted for visibility.

### 2.3.4. EPMA analysis

The major components (MgO, SiO<sub>2</sub>, and FeO) in the run products were obtained by the JEOL JXA-8200 electron probe microanalyzer (EPMA) with a wavelength-dispersive spectrometer (WDS) operated with an acceleration voltage of 15 kV, a beam current of 15 nA, and a counting time of 20 s. The detailed compositions were listed in Table 2 and Table 3 for ringwoodite and coexisted melt, respectively. The mass fraction of each component by EPMA would be affected by the Fe<sup>3+</sup>/Fe<sup>2+</sup> ratio, however, the atomic (Mg+Fe)/Si and Fe/(Fe+Mg) ratios listed in Table 2 and Table 3 should be independent from Fe<sup>3+</sup>/Fe<sup>2+</sup> ratio.

The Fe content in Pt-Rh capsule was also examined by EPMA. That was about 2 wt.% within 1 - 2 μm away from the inner wall of the capsule, and decreased to < 0.2 wt.% at ~6 μm away from the inner wall. Therefore, the Fe loss into the capsules was completely negligible.

## 3. Results

### 3.1. Infrared spectra

The FTIR spectra obtained in different regions of each capsule are very similar, indicating very homogeneous H<sub>2</sub>O distribution and therefore homogeneous temperature distribution within the capsule. The absorptions appear as a very broad band from 2600 to 3800 cm<sup>-1</sup> and small bands at 2450, 2530, and 2660 cm<sup>-1</sup>

**Table 2**  
Chemical composition of the recovered ringwoodite analyzed by electron microprobe. The data in parentheses are one standard deviation of the N analyzed points for each sample. The atomic number is normalized to O = 24. The Fe is assumed to be ferrous although up to 15~18% of total Fe can be ferric (McCammon et al., 2004).

Run. No.	Number of points	MgO (wt.%)	SiO <sub>2</sub> (wt.%)	FeO (wt.%)	Total (wt.%)	Mg (atomic)	Si (atomic)	Fe (atomic)	(Mg+Fe)/Si atomic ratio	Fe/(Mg+Fe) atomic ratio
H4775	14	55.81 (26)	42.29 (37)	–	98.10 (61)	11.901 (32)	6.049 (16)	–	1.967 (11)	–
H4784L	11	55.65 (80)	42.27 (41)	–	99.06 (48)	11.767 (139)	5.996 (70)	–	1.963 (46)	–
H4805	12	55.46 (35)	42.60 (20)	–	98.06 (51)	11.819 (28)	6.091 (14)	–	1.940 (9)	–
H4784H	12	55.03 (21)	42.56 (30)	–	97.63 (40)	11.777 (41)	6.110 (22)	–	1.928 (14)	–
H4793	13	55.23 (18)	42.30 (16)	–	97.56 (20)	11.835 (34)	6.081 (16)	–	1.946 (11)	–
H4800	19	54.69 (24)	42.80 (16)	–	97.52 (25)	11.705 (38)	6.145 (19)	–	1.905 (12)	–
H4754	10	50.49 (52)	40.03 (40)	8.31 (41)	98.82 (104)	11.132 (67)	5.921 (31)	1.027 (46)	2.054 (21)	8.45 (37)%
H4711	12	50.88 (29)	41.17 (13)	7.16 (40)	99.20 (29)	10.948 (54)	5.943 (20)	0.778 (43)	1.973 (12)	6.63 (37)%
S6985	12	50.36 (28)	40.97 (24)	8.67 (25)	100.01 (35)	10.802 (59)	5.895 (28)	0.939 (26)	1.992 (18)	8.00 (23)%
H4698	15	50.13 (39)	41.16 (23)	7.27 (35)	98.56 (35)	10.853 (78)	5.977 (28)	0.795 (38)	1.949 (19)	6.82 (34)%
S7011	13	52.05 (30)	41.35 (24)	5.44 (47)	98.84 (29)	11.190 (68)	5.963 (24)	0.590 (51)	1.976 (14)	5.01 (43)%
H4723	21	51.52 (23)	40.95 (20)	6.33 (13)	98.79 (23)	11.114 (46)	5.926(26)	0.689 (14)	1.992 (17)	5.84 (11)%
H4720	15	49.70 (36)	41.48 (27)	6.96 (32)	98.13 (27)	10.782 (71)	6.037 (34)	0.762 (36)	1.912 (21)	6.60 (31)%
S7051	17	53.95 (67)	41.01 (61)	3.55 (9)	98.52 (20)	11.596 (160)	5.913 (79)	0.386 (9)	2.027 (54)	3.22 (9)%
H4762	12	47.63 (13)	40.22 (12)	11.77 (20)	99.62 (32)	10.345 (21)	5.860 (13)	1.290 (20)	1.986 (8)	11.09 (17)%

**Table 3**  
Chemical composition of the melt analyzed by electron microprobe. The data in parentheses are one standard deviation of the N analyzed points for each sample. The atomic number is normalized to O = 24. The Fe is assumed to be ferrous.

Run. No.	Number of points	MgO (wt.%)	SiO <sub>2</sub> (wt.%)	FeO (wt.%)	Total (wt.%)	Mg (atomic)	Si (atomic)	Fe (atomic)	(Mg+Fe)/Si atomic ratio	Fe/(Mg+Fe) atomic ratio
H4775	9	43.3 (9)	27.6 (24)	–	70.9 (28)	12.96 (47)	5.52 (24)	–	2.35 (18)	–
H4784L	12	42.2 (15)	19.1 (7)	–	61.4 (18)	14.91 (22)	4.53 (11)	–	3.30 (13)	–
H4805	13	42.7 (9)	33.8 (8)	–	76.5 (14)	11.64 (17)	6.18 (9)	–	1.89 (5)	–
H4784H	15	41.1 (11)	25.7 (15)	–	66.9 (9)	13.04 (48)	5.47 (24)	–	2.39 (19)	–
H4793	5	47.6 (14)	35.4 (37)	–	83.1 (42)	12.03 (64)	5.98 (32)	–	2.02 (22)	–
H4800	11	37.8 (16)	25.2 (11)	–	63.2 (13)	12.65 (48)	5.66 (24)	–	2.24 (18)	–
H4754	8	34.0 (14)	22.3 (12)	19.7 (19)	76.0 (30)	10.89 (39)	4.79 (16)	3.53 (28)	3.01 (17)	24.5 (19)%
H4711	11	37.1 (12)	34.2 (8)	16.5 (4)	87.7 (4)	9.33 (29)	5.76 (13)	2.10 (6)	1.98 (9)	18.4 (7)%
S6985	14	39.1 (1)	27.1 (4)	12.3 (3)	78.5 (6)	11.08 (8)	5.14 (4)	1.76 (4)	2.50 (3)	13.7 (3)%
H4698	14	36.8 (8)	32.2 (5)	10.8 (2)	79.7 (11)	10.02 (14)	5.88 (7)	1.48 (2)	1.96 (5)	12.9 (2)%
S7011	15	38.3 (7)	31.2 (11)	10.9 (3)	80.5 (12)	10.40 (17)	5.68 (11)	1.49 (6)	2.10 (8)	12.6 (4)%
H4723	13	36.8 (7)	26.0 (8)	13.7 (3)	76.5 (7)	10.75 (23)	5.11 (13)	2.02 (5)	2.50 (11)	15.8 (3)%
H4720	10	34.6 (7)	20.4 (6)	17.9 (4)	72.8 (7)	11.01 (18)	4.34 (10)	2.87 (7)	3.20 (11)	20.7 (5)%
S7051	14	39.9 (11)	32.1 (8)	9.7 (3)	81.6 (16)	10.60 (15)	5.72 (8)	1.30 (6)	2.08 (6)	10.9 (5)%
H4762	10	29.9 (8)	26.8 (5)	27.3 (4)	84.0 (7)	8.29 (18)	4.99 (8)	3.83 (8)	2.43 (7)	31.6 (8)%

(Fig. 2). The absorption band at 3680 cm<sup>-1</sup> appears at C<sub>H<sub>2</sub>O</sub><sup>rw</sup> > ~1.0 wt.%, and is typically sharper in Fe-free ringwoodite than Fe-bearing one. These features agree with those reported previously (e.g., Bolfan-Casanova et al., 2018; Keppler and Bolfan-Casanova, 2006; Panero et al., 2013; Pearson et al., 2014; Smyth et al., 2003). The absorptions at 3120 cm<sup>-1</sup> appear as smooth peaks without noise, indicating no photon saturation in FTIR analyses.

### 3.2. C<sub>H<sub>2</sub>O</sub><sup>rw</sup> in the run products

For Fe-bearing system, the initial H<sub>2</sub>O and Fe contents in the starting materials vary from 1.5 to 22% and Fo75 to Fo90, respectively. In the run products, with increasing temperature from 1600 to 2000 K, the C<sub>H<sub>2</sub>O</sub><sup>rw</sup> systematically decreases from 1.50 to ~1.15 wt.% for starting material of Fo90 + 15% H<sub>2</sub>O. By reducing the initial H<sub>2</sub>O from 15 to 1.5%, C<sub>H<sub>2</sub>O</sub><sup>rw</sup> decreases almost proportionally. However, the C<sub>H<sub>2</sub>O</sub><sup>rw</sup> from 15 and 22 wt.% initial H<sub>2</sub>O runs are nearly identical at 2000 K (Table 1, Fig. 4). Adding more Fe in the starting material (Fo75) does not change C<sub>H<sub>2</sub>O</sub><sup>rw</sup> significantly at 2000 K (Fig. 4, 5). Note that as mentioned in section 2.3, the above C<sub>H<sub>2</sub>O</sub><sup>rw</sup> values are lowered by 27% for Fe-bearing system based on Bolfan-Casanova et al. (2018) FTIR calibration as listed in Table 1.

For Fe-free system, three sets of experiments with different starting materials were performed: run a) Mg<sub>2</sub>SiO<sub>4</sub> + 5 wt.% H<sub>2</sub>O, run b) Mg<sub>2</sub>SiO<sub>4</sub> + 15 wt.% H<sub>2</sub>O, and run c) Mg<sub>2</sub>Si<sub>1.1</sub>O<sub>4.2</sub> + 5 wt.% H<sub>2</sub>O (SiO<sub>2</sub> rich to ensure the coexistence of three phases), and the run products appeared as coexisting of: a) ringwoodite + melt, b) ringwoodite + melt + (akimotoite), and c) ringwoodite + akimo-

toite + melt, respectively. The products of run (c) show C<sub>H<sub>2</sub>O</sub><sup>rw</sup> = 2.03 wt.% at 1800 K and 1.06 wt.% at 2000 K [or 1.71 and 0.89 wt.% with Bolfan-Casanova et al. (2018) FTIR calibration], which are essentially the same as those in run (b), but considerably higher than those in run (a) (1.33 wt.% at 1800 K and 0.58 wt.% at 2000 K) (Table 1, Fig. 4).

## 4. Discussion

### 4.1. (Mg+Fe)/Si ratio and hydrogen incorporation in ringwoodite

H<sub>2</sub>O is incorporated into (Mg,Fe)<sub>2</sub>SiO<sub>4</sub> polymorphs as protons in Mg (and Fe) and/or Si sites. In general, a proportion of protons in Mg and Si sites can be estimated based on the deviation of the (Mg+Fe)/Si atomic ratio (Mg/Si ratio in Fe-free system) from the ideal formula. This ratio in wadsleyite significantly decreases with increasing H<sub>2</sub>O content, therefore, the majority of protons are supposed to be in Mg sites (Demouchy et al., 2005; Inoue et al., 1995) (Fig. 6). In the case of ringwoodite, the Mg/Si ratios for our and for Ohtani et al. (2000)'s high-C<sub>H<sub>2</sub>O</sub><sup>rw</sup> and Fe-free samples are obviously higher than those of wadsleyite, and are plotted around the line where protons are incorporated in Mg and Si sites with a ratio of about 2:1 (3:1 if only use the data from this study) (Fig. 6). It agrees with neutron diffraction experiments (Purevjav et al., 2014), which suggested simultaneous hydration of Mg and Si sites in ringwoodite. The Hydration process is thus written as,



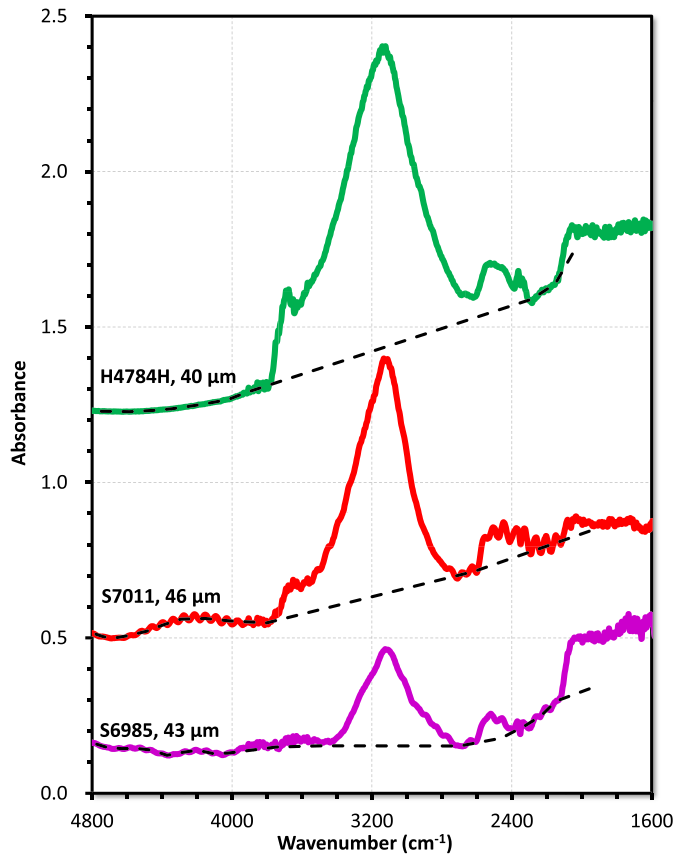


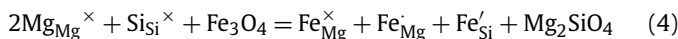
**Fig. 3.** Examples of baseline subtractions for FTIR spectra with various absorbances, corresponding different H<sub>2</sub>O contents. The spectra were vertically shifted for visibility.



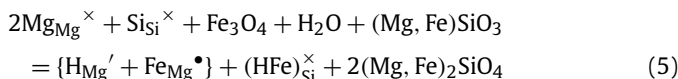
The reaction (2) occurs 4–6 times more than that of (3) and the ratio of [(2H)<sub>Mg</sub><sup>×</sup>] and [(4H)<sub>Si</sub><sup>×</sup>] is expected to be 4~6:1. [Here Kröger-Vink (1956) notation is used for the description of defect chemistry, e.g., (2H)<sub>Mg</sub><sup>×</sup> means two protons in the Mg site with neutral charge, Fe<sub>Si</sub><sup>'</sup> and Fe<sub>Mg</sub><sup>•</sup> indicate Fe ions substitute the Si and Mg sites, with effective charge of −1 and +1, respectively, and square brackets [A] denote the concentration of the species A.]

In contrast, the Fe-free samples with relatively low C<sub>H<sub>2</sub>O</sub><sup>rw</sup> (< ~1.0 wt.%) (This study; Bolfan-Casanova et al., 2018; Ohtani et al., 2000) generally follow the pure Mg site substitution, which means that the reaction (2) is probably more preferred when the C<sub>H<sub>2</sub>O</sub><sup>rw</sup> is low. The substitution mechanism of reaction (3) occurs with increasing of C<sub>H<sub>2</sub>O</sub><sup>rw</sup>.

About 15–18% of total Fe is ferric in hydrous ringwoodite based on Mössbauer spectroscopy (McCammon et al., 2004). Because both ringwoodite and magnetite have the spinel structure, a certain proportion of (Mg,Fe)<sub>2</sub>SiO<sub>4</sub> should be substituted by Fe<sub>3</sub>O<sub>4</sub>,



The Fe<sup>3+</sup> related hydration process is thus considered as,



This hydration process may cause slightly higher (Mg+Fe)/Si ratio than Fe-free ringwoodite although such tendency was unclear in Fig. 6 due to the large scattering of data points for Fe-bearing samples.

## 4.2. H<sub>2</sub>O solubility in ringwoodite

### 4.2.1. Fe-bearing system

The C<sub>H<sub>2</sub>O</sub><sup>rw</sup> in Fe-bearing ringwoodite with 15 and 22 wt.% initial H<sub>2</sub>O are identical, and considerably higher than those with 1.5–5 wt.% initial H<sub>2</sub>O (Fig. 4). Clearly, the runs with 15–22 wt.% initial H<sub>2</sub>O should represent the H<sub>2</sub>O solubility in ringwoodite since C<sub>H<sub>2</sub>O</sub><sup>rw</sup> is independent from initial H<sub>2</sub>O content. Ringwoodite from the experiments with 1.5–5 wt.% initial H<sub>2</sub>O should be undersaturated. The H<sub>2</sub>O solubility is thus 1.15–1.50 wt.% at 1600 to 2000 K (0.84–1.09 wt.% based on Bolfan-Casanova et al., 2018's FTIR calibration). This value is comparable with that reported by Fei et al. (2017) at 1800 K, who used free water as H<sub>2</sub>O source (namely very high but unknown initial H<sub>2</sub>O). In contrast, it is 1.5–3.0 times higher than those reported previously who used only 3–5 wt.% initial H<sub>2</sub>O (Bolfan-Casanova et al., 2018; Kawamoto et al., 1996; Smyth et al., 2003) (Fig. 4). One may attribute this difference to the various analytical methods adopted in measuring the H<sub>2</sub>O contents [i.e. FTIR with various calibrations, ERDA, and SIMS]. As demonstrated in Bolfan-Casanova et al. (2018), however, only Paterson (1982)'s FTIR calibration, namely, Smyth et al. (2003) may have significantly underestimated the H<sub>2</sub>O solubility, whereas the other methods should have given comparable results (Fig. 4). Essentially, as demonstrated by our FTIR spectra (Fig. 2), C<sub>H<sub>2</sub>O</sub><sup>rw</sup> is limited by the initial H<sub>2</sub>O if it is low.

In the view of thermodynamics, although three phases coexisted (ringwoodite + akimotoite + melt), the composition of each phase (e.g. C<sub>H<sub>2</sub>O</sub><sup>rw</sup> in ringwoodite) should be fixed at a given pressure and temperature condition only in the three-component system (e.g. Demouchy et al., 2005). Since there are four/five components in the Fe-bearing experiments [MgO + SiO<sub>2</sub> + H<sub>2</sub>O + FeO (+Fe<sub>2</sub>O<sub>3</sub>)], there should be one or two more freedom. It is thus reasonable that C<sub>H<sub>2</sub>O</sub><sup>rw</sup> is initial- H<sub>2</sub>O dependent when it is below the solubility. As experimentally observed, if the initial H<sub>2</sub>O is low (1.5 ~ 5% H<sub>2</sub>O), C<sub>H<sub>2</sub>O</sub><sup>rw</sup> systematically increases with increasing initial H<sub>2</sub>O content. When the initial H<sub>2</sub>O is 15 ~ 22%, C<sub>H<sub>2</sub>O</sub><sup>rw</sup> reaches the solubility value and therefore it becomes independent from initial H<sub>2</sub>O content.

### 4.2.2. Fe-free system

There are three components (MgO-SiO<sub>2</sub>-H<sub>2</sub>O) in the Fe-free system. As far as three phases coexist, all the thermodynamic parameters of the system should be fixed at a given pressure and temperature condition. Namely, no matter how much H<sub>2</sub>O is added in the starting material, the C<sub>H<sub>2</sub>O</sub><sup>rw</sup> should remain unchanged when ringwoodite, akimotoite, and melt coexist. This turned out to be true in our experiments (Fig. 4, Table 1), i.e., the C<sub>H<sub>2</sub>O</sub><sup>rw</sup> in runs (b) and (c) are essentially the same, for which the bulk compositions of the starting materials are located within the ringwoodite-akimotoite-melt triangle in the compositional diagram (Fig. 7). Therefore, the H<sub>2</sub>O solubility in Fe-free ringwoodite should be ~2.0 and ~1.0 wt.% at 1800 and 2000 K, respectively, based on Koch-Müller and Rhede (2010) calibration, or ~1.7 and 0.9 wt.%, respectively, if use the relatively larger FTIR absorption coefficient reported by Bolfan-Casanova et al. (2018).

In contrast, the C<sub>H<sub>2</sub>O</sub><sup>rw</sup> obtained in runs (a) is only 1.33 and 0.58 wt.% at 1800 and 2000 K, respectively (0.49 and 1.12 wt.% based on Bolfan-Casanova et al.'s calibration), whereas Ohtani et al. (2000) obtained C<sub>H<sub>2</sub>O</sub><sup>rw</sup> of 0.2~0.3 wt.% at 1950–2070 K. These values are considerably lower than the H<sub>2</sub>O solubility determined by runs (b) and (c), and this difference is not related to the FTIR calibration methods because the infrared absorptions are clearly different as shown in Fig. 2. Since Mg<sub>2</sub>SiO<sub>4</sub> + 5% initial H<sub>2</sub>O was used as starting material and only two phases (ringwoodite + melt) coexisted in those low-C<sub>H<sub>2</sub>O</sub><sup>rw</sup> experiments, there should be one more freedom additional to pressure and temperature in

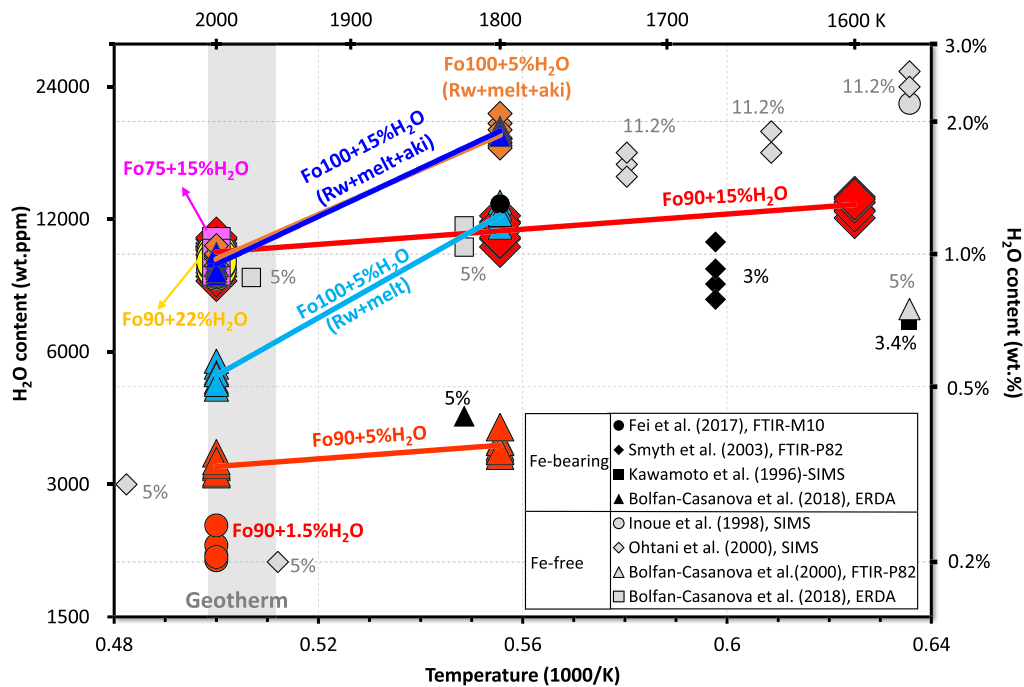


**Fig. 4.** Temperature dependence of H<sub>2</sub>O content or solubility in ringwoodite. The data sets labeled with Fo100+5%H<sub>2</sub>O (Mg<sub>2</sub>Si<sub>1.1</sub>O<sub>4.2</sub>), Fo100+15%H<sub>2</sub>O, Fo90+22%H<sub>2</sub>O, Fo90+15%H<sub>2</sub>O, and Fo75+15%H<sub>2</sub>O should represent the H<sub>2</sub>O solubility in ringwoodite. Each data point from this study is C<sub>H<sub>2</sub>O</sub><sup>rw</sup> from one single FTIR spectrum based on the average of Koch-Müller and Rhede (2010) and Bolfan-Casanova et al. (2018) calibrations. The percentages next to the data points are the initial H<sub>2</sub>O contents in the starting materials. The geotherm in the lower mantle transition zone is taken from Katsura et al. (2010). SIMS: secondary ion mass spectrometry. FTIR-P82: FTIR with Paterson (1982) calibration. FTIR-M10: FTIR with Koch-Müller and Rhede (2010) calibration. ERDA: elastic recoil detection analysis (Bolfan-Casanova et al., 2018). Although more data were reported in Bolfan-Casanova et al. (2018) and Smyth et al. (2003), only C<sub>H<sub>2</sub>O</sub><sup>rw</sup> for ringwoodite that coexisted with melts were shown in the figure since C<sub>H<sub>2</sub>O</sub><sup>rw</sup> from other runs cannot represent the H<sub>2</sub>O solubility.

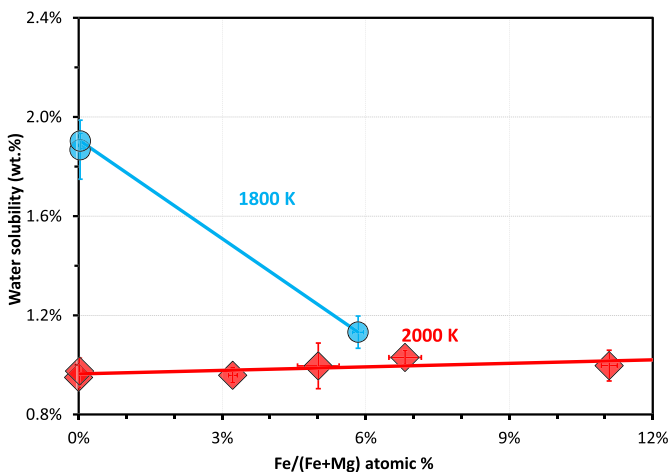


**Fig. 5.** Fe content dependence of H<sub>2</sub>O solubility in ringwoodite based on the average of Koch-Müller and Rhede (2010) and Bolfan-Casanova et al. (2018) calibrations. Although the Fe/(Fe+Mg) atomic ratio in the starting material for Fe-bearing system was 10% or 25%, that in ringwoodite was less than 11% since Fe prefers to participate into melt rather than solid.

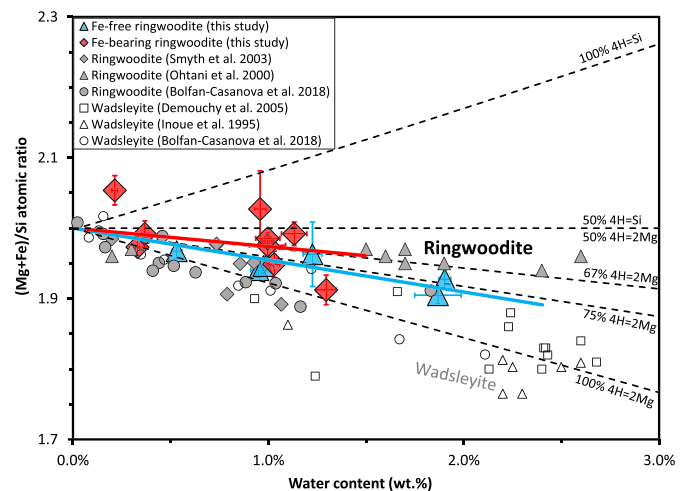


**Fig. 6.** (Mg+Fe)/Si atomic ratio in ringwoodite as a function of H<sub>2</sub>O content from the average of Koch-Müller and Rhede (2010) and Bolfan-Casanova et al. (2018) calibrations. The ratio in wadsleyite is also shown for comparison. The interception of fitting lines on vertical axis is set to (Mg+Fe)/Si = 2.0. The dash lines represent the theoretical calculations with 100% proton following (4H)<sub>2</sub>MgSiO<sub>4</sub> substitution mechanism, 100% following Mg<sub>2</sub>(4H)<sub>2</sub>SiO<sub>4</sub> substitution mechanism, 50:50, 67:33, and 75:25 of (4H)<sub>2</sub>MgSiO<sub>4</sub> and Mg<sub>2</sub>(4H)<sub>2</sub>SiO<sub>4</sub> substitution mechanisms. The samples of Inoue et al. (1998), Ohtani et al. (2000), and Demouchy et al. (2005) are all Fe-free, whereas Bolfan-Casanova et al. (2018) of both Fe-free and Fe-bearing systems.

the MgO-SiO<sub>2</sub>-H<sub>2</sub>O system. Namely, those samples may not represent the H<sub>2</sub>O solubility in Fe-free ringwoodite. Because run (a) is not buffered by silica-rich phases such as akimotoite or stishovite, the Mg/Si ratio is thus slightly higher, which could be the reason for the low C<sub>H<sub>2</sub>O</sub><sup>rw</sup> as far as the majority of protons is stored in Mg vacancies as discussed above. It is speculated that the melt composition varies with initial H<sub>2</sub>O in the ringwoodite + melt two-phase region of the phase diagram, leading to various C<sub>H<sub>2</sub>O</sub><sup>rw</sup> with the initial composition (Fig. 7). By adding either more H<sub>2</sub>O or more SiO<sub>2</sub> in the Mg<sub>2</sub>SiO<sub>4</sub> + 5% H<sub>2</sub>O system, the bulk composition

would be located in the ringwoodite + akimotoite + melt three-phase region and then the ringwoodite would be H<sub>2</sub>O-saturated.

Quite recently, Bolfan-Casanova et al. (2018) reported C<sub>H<sub>2</sub>O</sub><sup>rw</sup> = 0.89 wt.% at 1970 K in Fe-free ringwoodite. It is identical to the C<sub>H<sub>2</sub>O</sub><sup>rw</sup> obtained in run (b) and (c) by considering the 16% lower of C<sub>H<sub>2</sub>O</sub><sup>rw</sup> with Bolfan-Casanova et al. (2018) calibration even though Mg<sub>2</sub>SiO<sub>4</sub> + 5% initial H<sub>2</sub>O were used in their experiments. It is

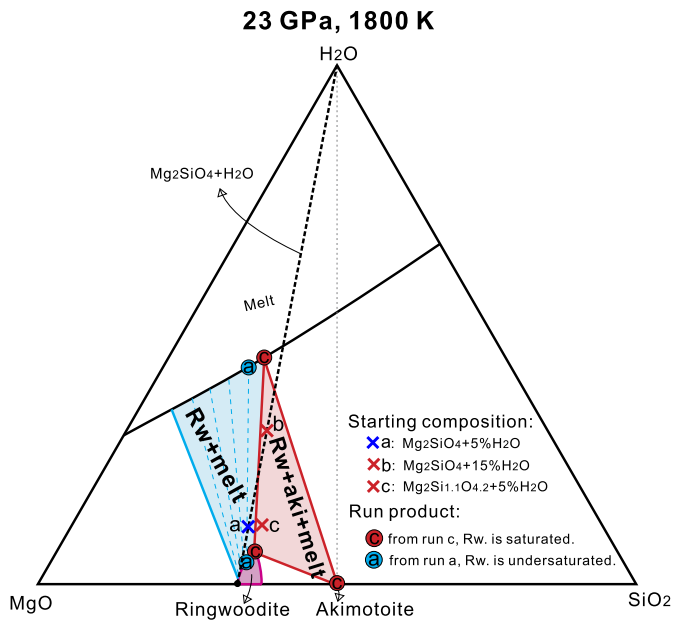


**Fig. 7.** Ternary phase diagram in the MgO-SiO<sub>2</sub>-H<sub>2</sub>O system at 23 GPa, 1800 K based on the runs H4784L, H4784H, and H4800. The red and blue area represent the three-phase (ringwoodite + akimotoite + melt) and two-phase (ringwoodite + melt) coexisting regions, respectively. The H<sub>2</sub>O concentrations in the melt phases were estimated from initial H<sub>2</sub>O contents in the starting materials and melt fractions of the run products. The cross and circle symbols denote the compositions of the starting materials and run products, respectively.

actually not against our results because their brucite was CO<sub>2</sub>-contaminated, therefore, the starting material could be actually slightly SiO<sub>2</sub> rich.

#### 4.2.3. Temperature and Fe content dependences of H<sub>2</sub>O solubility

Temperature has significant effect on the H<sub>2</sub>O solubility in Fe-free ringwoodite. With increasing temperature from 1800 to 2000 K, the H<sub>2</sub>O solubility decreases by ~50%. In contrast, the H<sub>2</sub>O solubility is less sensitive to temperature in Fe-bearing system. From 1600 to 2000 K, the H<sub>2</sub>O solubility decreases from 1.50 to 1.15 wt.% (1.09 to 0.84 wt.% based on Bolfan-Casanova et al.'s calibration) (Fig. 4; Table 1). Note that a crossover of Fo90 and Fo100 lines occurs at ~1950 K (Fig. 4), however, it is probably caused by experimental uncertainty because the difference of H<sub>2</sub>O solubility between Fe-free and Fe-bearing samples are less than ~15% at 2000 K (1.03~1.06 vs. 1.11~1.19 wt.%) (Table 1).

The H<sub>2</sub>O solubility is nearly independent from Fe content at 2000 K, whereas that at 1800 K in Fe-bearing ringwoodite is much lower than Fe-free system (Fig. 4, Fig. 5). Namely, Fe-free ringwoodite can store more H<sub>2</sub>O than Fe-bearing one at < 2000 K. Since silicate melt and H<sub>2</sub>O are miscible under mantle transition zone conditions (Bureau and Keppler, 1999; Demouchy et al., 2005; Kawamoto et al., 2004), the H<sub>2</sub>O solubility in ringwoodite is controlled by the H<sub>2</sub>O activity in the coexisting hydrous melt (e.g., Demouchy et al., 2005; Keppler and Bolfan-Casanova, 2006). By adding Fe<sub>2</sub>SiO<sub>4</sub> component, the melt fraction may increase slightly because the melting temperature of (Mg,Fe)<sub>2</sub>SiO<sub>4</sub> decreases with increasing Fe/(Mg+Fe) ratio. As a result, the H<sub>2</sub>O activity in melt decreases, which causes the lower H<sub>2</sub>O solubility in Fe-bearing ringwoodite.

Additionally, variation of oxygen fugacity ( $f_{O_2}$ ) may affect the Fe<sup>3+</sup>/Fe<sup>2+</sup> ratio in Fe-bearing ringwoodite. Based on Mössbauer spectroscopy analysis (McCammon et al., 2004), however, Fe<sup>3+</sup>/Fe<sup>2+</sup> ratio is independent from  $C_{H_2O}^{TW}$ , namely, the H<sub>2</sub>O solubility should be independent from  $f_{O_2}$  as well. This is also proved

by the identical  $C_{H_2O}^{TW}$  obtained in this study without controlling  $f_{O_2}$  with that in Fei et al. (2017) buffered by Re foils (Fig. 4).

#### 4.3. Water in the mantle transition zone

Wadsleyite and ringwoodite are the dominant minerals in the upper (410-520 km depth) and lower (520-660 km depth) part of the mantle transition zone, respectively (e.g., Ringwood, 1991). The H<sub>2</sub>O solubility of wadsleyite at 1850-1900 K (upper mantle transition zone geotherm) has been estimated to be 0.8-1.1 wt.% (Demouchy et al., 2005; Kawamoto et al., 1996; Litasov et al., 2011; Sun et al., 2018), (Fig. 4). Meanwhile, even at 1950-2000 K, corresponding to the lower mantle transition zone geotherm (Katsura et al., 2010), 1.1~1.2 wt.% H<sub>2</sub>O based on Koch-Müller and Rhede's calibration, or 0.8~0.9 wt.% H<sub>2</sub>O based on Bolfan-Casanova et al.'s calibration, can be stored within the crystals of iron-bearing ringwoodite, which is 3-6 times higher than that reported previously (Ohtani et al., 2000). Namely, both the upper and lower mantle transition zone can store about 0.8~1.2 wt.% H<sub>2</sub>O.

Of course H<sub>2</sub>O solubility of minerals does not represent the actual H<sub>2</sub>O content in the mantle transition zone. The question is whether the mantle transition zone is H<sub>2</sub>O rich or not. Based on the comparison of magnetotellurically-interpreted electrical conductivity with the laboratory-measured conductivity of wadsleyite and ringwoodite, it has been proposed that the mantle transition zone contains < 0.1 ~ 1.0 wt.% H<sub>2</sub>O (Huang et al., 2005; Karato, 2011; Kelbert et al., 2009; Yoshino et al., 2008). However, due to the difficulties of conductivity measurements, the estimated H<sub>2</sub>O contents in the mantle transition zone by different groups range by nearly one order of magnitude. Additionally, most of the H<sub>2</sub>O-related conductivity measurements only focus on the free-proton controlled conduction mechanism at low temperature regime (typically < 1500 K). It should be inappropriate for estimation of H<sub>2</sub>O content in the mantle transition zone due to the conduction mechanism transitions at higher temperatures (Yoshino et al., 2008).

From seismic data (e.g., Houser, 2016; Meier et al., 2009), a relatively dry mantle transition zone (< 0.6 wt.% H<sub>2</sub>O) has been proposed based on the reduction of sound velocity by the hydration of wadsleyite and ringwoodite (Jacobsen et al., 2004; Mao et al., 2008). Nevertheless, recent experiments (Buchen et al., 2018; Schulze et al., 2018) demonstrated that the elasticity of both wadsleyite and ringwoodite are insensitive to H<sub>2</sub>O contents under mantle transition zone conditions, therefore, seismic observations would be unable to tell the hydration states in the mantle transition zone.

Since the viscosity of nominally anhydrous minerals is lowered by hydration, Fei et al. (2017) investigated the viscosity contrast between ringwoodite and bridgmanite and concluded that the mantle transition zone should contain ≥ 1.0 wt.% H<sub>2</sub>O to fit the geophysically interpreted mantle viscosity profiles. According to the high H<sub>2</sub>O solubility reported here, ringwoodite in the mantle transition zone can store 0.8~1.2 wt.% H<sub>2</sub>O upon different calibration methods, which agrees well with the water-rich mantle transition zone inferred from mineral viscosity (e.g., Fei et al., 2017) and the ringwoodite inclusion within the natural diamond crystal (Pearson et al., 2014). Therefore, by assuming the volume fraction of 60% wadsleyite/ringwoodite and 40% majoritic garnet, the transition zone from 410-660 km depth may store about twice of the total mass of oceanic water on the Earth's surface.

#### Declaration of competing interest

The authors declare that they have no known competing financial interests or personal relationships that could have appeared to influence the work reported in this paper.

## Acknowledgements

We appreciate the help of H. Fischer for high-pressure cell assembly preparation, R. Njul for sample polishing, R. Huang and D. Krauß for EPMA analysis, and L. Wang for discussion. Comments from three anonymous reviewers are helpful to improve the manuscript. This work is funded by the Deutsche Forschungsgemeinschaft (DFG) to T. Katsura (KA3434/3-2, KA3434/7-1, KA3434/8-1, and KA3434/9-1, KA3434/11-1, KA3434/12-1).

## References

- Bercovici, D., Karato, S.I., 2003. Whole-mantle convection and the transition-zone water filter. *Nature* 425, 39–44.
- Bolfan-Casanova, N., Keppler, H., Rubie, D.C., 2000. Water partitioning between nominally anhydrous minerals in the MgO-SiO<sub>2</sub>-H<sub>2</sub>O system up to 24 GPa: implications for the distribution of water in the Earth's mantle. *Earth Planet. Sci. Lett.* 182, 209–221.
- Bolfan-Casanova, N., Schiavi, F., Novella, D., Bureau, H., Raepsaet, C., Khodja, H., Demouchy, S., 2018. Examination of water quantification and incorporation in transition zone minerals: wadsleyite, ringwoodite, and phase D using ERDA (elastic recoil detection analysis). *Front. Earth Sci.* 6, 75. <https://doi.org/10.3389/feart.2018.00075>.
- Buchen, J., Marquardt, H., Speziale, S., Kawazoe, T., Boffa-Ballaran, T., Kurnosov, A., 2018. High-pressure single-crystal elasticity of wadsleyite and the seismic signature of water in the shallow transition zone. *Earth Planet. Sci. Lett.* 498, 77–87.
- Bureau, H., Keppler, H., 1999. Complete miscibility between silicate melts and hydrous fluids in the upper mantle: experimental evidence and geochemical implications. *Earth Planet. Sci. Lett.* 165, 187–196.
- Demouchy, S., Deloule, E., Frost, D.H., Keppler, H., 2005. Pressure and temperature dependence of water solubility in Fe-free wadsleyite. *Am. Mineral.* 90, 1084–1091.
- Fei, H., Yamazaki, D., Sakurai, M., Miyajima, N., Ohfuji, H., Katsura, T., Yamamoto, T., 2017. A nearly water-saturated mantle transition zone inferred from mineral viscosity. *Sci. Adv.* 3, e1603024.
- Hirschmann, M.M., 2006. Water, melting, and the deep Earth H<sub>2</sub>O cycle. *Annu. Rev. Earth Planet. Sci.* 34, 629–653.
- Houser, C., 2016. Global seismic data reveal little water in the mantle transition zone. *Earth Planet. Sci. Lett.* 448, 94–101.
- Huang, X., Xu, Y., Karato, S.I., 2005. Water content in the transition zone from electrical conductivity of wadsleyite and ringwoodite. *Nature* 434, 746–749.
- Inoue, T., Hisayoshi, Y., Kudoh, Y., 1995. Hydrous modified spinel, Mg<sub>1.75</sub>SiH<sub>0.5</sub>O<sub>4</sub>: a new water reservoir in the mantle transition region. *Geophys. Res. Lett.* 22, 117–120.
- Inoue, T., Weidner, D.J., Northrup, P.A., Parise, J.B., 1998. Elastic properties of hydrous ringwoodite ( $\gamma$ -phase) in Mg<sub>2</sub>SiO<sub>4</sub>. *Earth Planet. Sci. Lett.* 160, 107–113.
- Jacobsen, S.D., Smyth, J.R., Spetzler, H., Holl, C.M., Frost, D.J., 2004. Sound velocities and elastic constants of iron-bearing hydrous ringwoodite. *Phys. Earth Planet. Inter.* 143, 47–56.
- Karato, S.I., 2011. Water distribution across the mantle transition zone and its implications for global material circulation. *Earth Planet. Sci. Lett.* 301, 413–423.
- Katsura, T., Yoneda, A., Yamazaki, D., Yoshino, T., Ito, E., 2010. Adiabatic temperature profile in the mantle. *Phys. Earth Planet. Inter.* 183, 212–218.
- Kawamoto, T., Hervig, R.L., Holloway, J.R., 1996. Experimental evidence for a hydrous transition zone in the early Earth's mantle. *Earth Planet. Sci. Lett.* 142, 587–592.
- Kawamoto, T., Matsukage, K.N., Mibe, K., Isshiki, M., Nishimura, K., Ishimatsu, N., Ono, S., 2004. Mg/Si ratios of aqueous fluids coexisting with forsterite and enstatite based on phase relations in the Mg<sub>2</sub>SiO<sub>4</sub>-SiO<sub>2</sub>-H<sub>2</sub>O system. *Am. Mineral.* 89, 1433–1437.
- Kelbert, A., Schultz, A., Egbert, G., 2009. Global electromagnetic induction constraints on transition-zone water content variations. *Nature* 460, 1003–1006.
- Keppler, H., Bolfan-Casanova, N., 2006. Thermodynamics of water solubility and partitioning. *Rev. Mineral. Geochem.* 62, 193–230.
- Koch-Müller, M., Rhede, D., 2010. IR absorption coefficients for water in nominally anhydrous high-pressure minerals. *Am. Mineral.* 95, 770–775.
- Kohlstedt, D.L., Keppler, H., Rubie, D.C., 1996. Solubility of water in the  $\alpha$ ,  $\beta$ , and  $\gamma$  phases of (Mg,Fe)<sub>2</sub>SiO<sub>4</sub>. *Contrib. Mineral. Petrol.* 123, 345–357.
- Kröger, F.A., Vink, H.J., 1956. Relations between the concentrations of imperfections in crystalline solids. *Solid State Phys.* 3, 307–435.
- Litasov, K.D., Shatskiy, A., Ohtani, E., Katsura, T., 2011. Systematic study of hydrogen incorporation into Fe-free wadsleyite. *Phys. Chem. Miner.* 38, 75–84.
- Mao, Z., Jacobsen, S.D., Jiang, F., Smyth, J.R., Holl, C.M., Duffy, T.S., 2008. Elasticity of hydrous wadsleyite to 12 GPa: implications for Earth's transition zone. *Geophys. Res. Lett.* 35, L21305. <https://doi.org/10.1029/2008GL035618>.
- Meier, U., Trampert, J., Curtis, A., 2009. Global variations of temperature and water content in the mantle transition zone from higher mode surface waves. *Earth Planet. Sci. Lett.* 282, 91–101.
- McCammon, C.A., Frost, D.J., Smyth, J.R., Laustsen, H.M.S., Kawamoto, T., Ross, N.L., van Aken, P.A., 2004. Oxidization state of iron in hydrous mantle phases: implications for subduction and mantle oxygen fugacity. *Phys. Earth Planet. Inter.* 143, 157–169.
- Ohtani, E., Mizobata, H., Yurimoto, H., 2000. Stability of dense hydrous magnesium silicate phases in the systems Mg<sub>2</sub>SiO<sub>4</sub>-H<sub>2</sub>O and MgSiO<sub>3</sub>-H<sub>2</sub>O at pressures up to 27 GPa. *Phys. Chem. Miner.* 27, 533–544.
- Panero, W.R., Smyth, J.R., Pigott, J.S., Liu, Z., Frost, D.J., 2013. Hydrous ringwoodite to 5 K and 35 GPa: multiple hydrogen bonding sites resolved with FTIR spectroscopy. *Am. Mineral.* 98, 637–642.
- Paterson, M.S., 1982. The determination of hydroxyl by infrared absorption in quartz, silicate glasses and similar minerals. *Bull. Mineral.* 105, 20–29.
- Pearson, D.G., Brenker, F.E., Nestola, F., McNeil, J., Nasdala, L., Hutchison, M.T., Matveev, S., Mather, M., Silversmit, G., Schmitz, S., Vekemans, B., Vincze, L., 2014. Hydrous mantle transition zone indicated by ringwoodite included within diamond. *Nature* 507, 221–224.
- Purevjav, N., Okuchi, T., Tomioka, N., Abe, J., Harjo, S., 2014. Hydrogen site analysis of hydrous ringwoodite in mantle transition zone by pulsed neutron diffraction. *Geophys. Res. Lett.* 41, 6718–6724.
- Ringwood, A.E., 1991. Phase transformations and their bearing on the constitution and dynamics of the mantle. *Geochim. Cosmochim. Acta* 55, 2083–2110.
- Schulze, K., Marquardt, H., Kawazoe, T., Boffa-Ballaran, T., McCammon, C., Koch-Müller, M., Kurnosov, A., Marquardt, K., 2018. Seismically invisible water in Earth's transition zone? *Earth Planet. Sci. Lett.* 498, 9–16.
- Smyth, J.R., Holl, C.M., Frost, D.J., Jacobsen, S.D., Langenhorst, F., McCammon, C.A., 2003. Structural systematics of hydrous ringwoodite and water in Earth's interior. *Am. Mineral.* 88, 1402–1407.
- Sun, W., Yoshino, T., Sakamoto, N., Yurimoto, H., 2015. Hydrogen self-diffusivity in single crystal ringwoodite: implications for water content and distribution in the mantle transition zone. *Geophys. Res. Lett.* 42, 6582–6589.
- Sun, W., Yoshino, T., Sakamoto, N., Yurimoto, H., 2018. Supercritical fluid in the mantle transition zone deduced from H-D interdiffusion of wadsleyite. *Earth Planet. Sci. Lett.* 484, 309–317.
- Thio, V., Cobden, L., Trampert, J., 2016. Seismic signature of a hydrous mantle transition zone. *Phys. Earth Planet. Inter.* 250, 46–63.
- Tschauner, O., Huang, S., Greenberg, E., Prakapenka, V.B., Ma, C., Rossman, G.R., Shen, A.H., Zhang, D., Newville, M., Lanzirotti, A., Tait, K., 2018. Ice-VII inclusions in diamonds: evidence for aqueous fluid in Earth's deep mantle. *Science* 359, 1136–1139.
- Yoshino, T., Manthilake, G., Matsuzaki, T., Katsura, T., 2008. Dry mantle transition zone inferred from the conductivity of wadsleyite and ringwoodite. *Nature* 451, 326–329.